Unravelling Mechanistic Differences in Optical and Electrical Sensors: Time-Resolved Operando UV-VIS Spectroscopy of p-Type Perovskite Gas Sensors

*Maximilian Pfeiffer, Christian Hess**

TU Darmstadt, Eduard Zintl Institute of Inorganic and Physical Chemistry, Peter-Grünberg-Str.8, 64287 Darmstadt, Germany

KEYWORDS

Chemiresistive gas sensors, optical gas sensors, $LaFeO_3$, ethanol, *operando* UV-VIS spectroscopy, free carrier absorption

ABSTRACT

To gain a deeper understanding of p-type chemiresistive and gasochromic sensor materials, $LaFeO_3$ and $SmFeO_3$ were investigated using time-resolved *operando* UV-VIS spectroscopy. A qualitative match in the electrical conductance and optical absorbance below the band edge was observed. The two properties are connected by changes in the electron hole concentration caused by the sensor surface reaction with ethanol, leading to a decrease in both conductance and free carrier absorption. Quantitative differences between the conductance and free carrier absorption behavior are explained based on surface effects caused by surface band bending and surface adsorbates, which lead to significant changes in conductance but are only of minor importance for changes in the free carrier absorption. Our results demonstrate the potential of time-resolved *operando* UV-VIS spectroscopy to develop a detailed mechanistic understanding of chemiresistive and gasochromic sensors, by discriminating between surface and bulk effects, and to combine their use for future gas sensor development.

1. Introduction

Sensors are ubiquitous in many products of daily life and continue to gain importance in the context of the Internet of Things (IoT), in which the sensors share one joint network, allowing their linkage and exchange of individual measurement signals.[1] As a prominent part of this, gas sensors are of great importance for safety engineering and gas-phase analysis in the qualitative and quantitative determination of toxic and explosive gases in ambient and exhaled air.[2] A large proportion of these gas sensors is based on semiconducting metal oxides,[3] which show changes in their electrical and optical properties when the analyte is present.[4] In chemiresistive gas sensors,[2] changes in electrical resistance are recorded, and in optical, gasochromic gas sensors,[5] changes in absorbance of visible light are recorded.

Although materials such as WO_3 or NiO show changes in both electrical and optical properties when exposed to reducing gases (e.g. such as CO[6,7] or H_2[8]), and are therefore used as both electrical and optical gas sensors, the underlying sensing mechanisms have been studied mostly separately. To gain an in-depth understanding of the sensing mechanism of gas sensors that are both chemiresistive and gasochromic, and to unravel similarities, differences and possibly synergistic effects between the two types of sensing, systematic *operando* spectroscopic studies that simultaneously measure the electrical and optical changes during sensor operation are needed.

Perovskites such as $LaFeO_3$ are promising materials for various applications, for example, solid-oxide cells,[9] photovoltaic cells,[10] and gas sensors.[11] As a sensor material, $LaFeO_3$ has shown good sensitivity and selectivity for volatile organic substances.[11] For example, $LaFeO_3$ showed high sensitivity to acetylenes with simultaneously high selectivity compared to ethylene and other saturated and unsaturated hydrocarbons,[11] as well as CO, CO_2 and H_2.[12] The sensing properties of these perovskites can be modified by exchanging one or both cations,[11] as well as loading with

noble metals such as silver.[13,14] Since $LaFeO_3$ and $SmFeO_3$ are p-type semiconducting metal oxides, in contrast to the metal oxide materials such as SnO_2 that have been much studied as gas sensors[4], a study of the two materials additionally helps to deepen the comparatively lower fundamental understanding of p-type semiconducting gas sensor materials[15].

The aim of this work is to use continuous, time-resolved *operando* UV-VIS spectroscopy on the time scale of one second (DC resistance) to one minute (UV-VIS) to simultaneously investigate changes in electrical conductance and UV-VIS absorbance of $LaFeO_3$ and $SmFeO_3$ gas sensors during exposure to 250 ppm ethanol under working conditions, providing direct access to mechanistic information in one setup. Such a time-resolved *operando* UV-VIS spectroscopy approach has not previously been applied to metal-oxide gas sensors that show simultaneous electrical and optical sensor responses, despite the potential of even steady-state *operando* UV-VIS spectroscopy. Recent studies showed that UV-VIS spectra can provide complementary information to the widely used vibrational spectroscopic approaches[11,16] to study gas sensors[16,17] and catalysts[18–20] under *in situ* and *operando* conditions, providing new insights into their fundamental sensor- and surface reaction mechanisms, respectively. For example, *operando* UV-VIS spectra of tin oxide gas sensors during CO[17] and ethanol[16] gas sensing demonstrated an increase in the concentration of free charge carriers in the conduction band due to the formation and ionization of oxygen vacancies.

2. Experimental section

2.1. Material preparation. The $LaFeO_3$ and $SmFeO_3$ samples were synthesized by a sol-gel-technique, using stoichiometric amounts of $La(NO_3)_3 \cdot 6H_2O$ (Fluka, ≥99.0%) or $Sm(NO_3)_3 \cdot 6H_2O$ (Acros Organics, ≥99.9%) and $Fe(NO_3)_3 \cdot 9H_2O$ (Fluka, ≥99.0%). The metal nitrites were dissolved in deionized water together with citric acid in a 1:1 ratio of metal ions to citric acid. After 1 h of stirring, ammonium hydroxide was added under vigorous stirring to neutralize the precursor solution. The resulting gel was dried at 90 °C for 4 h and then calcined at 600 °C for 2 h.[11]

2.2. Sensor preparation. The transducers consist of an aluminum oxide substrate screen-printed with a platinum heater on one side and platinum electrodes for the four-point resistance measurement on the other. 30 mg of the respective sensor material was dispersed in 90 µL of deionized water under ultrasonic bath treatment. The suspension was dropped stepwise onto the electrodes. After each step, the supernatant water evaporated at room temperature. When the deposition of the suspension was finished, the transducer was dried at 85 °C for 24 h and calcined stepwise at 500 °C, 600 °C and 500 °C for 10 min each.

2.3. *Ex situ* characterization. XRD patterns of the powder samples were recorded using a Stoe Stadi P diffractometer with a Ge(111)-monochromator, Cu $K_{\alpha 1}$ radiation (λ = 1.54060 Å, 40 mA), and a MYTHEN-1K Dectris detector. The samples were prepared between two X-ray amorphous polymer foils on a planar sample support.

Ex situ Raman spectra were acquired in a 180° backscattering geometry using a 20× objective (Olympus SLMPLN20x) and an excitation wavelength of 632.8 nm using a diode laser (Ondax).

The laser power at the sample was about 5 mW. A HoloSpec f/1.8i Raman spectrometer (Kaiser Optical Systems) with an axial transmission grating and a Peltier-cooled charge-coupled device (CCD) was used as the detector. The spectrometer has a spectral resolution specified as 5 cm^{-1}. Raman spectra were collected with an exposure time of 80 s, using an auto new dark and a cosmic ray filter for each measurement, leading to total measuring time of 320 s.

2.4. *Operando* UV-VIS spectroscopy. UV-VIS spectra under *operando* conditions were recorded in a custom-built *operando* cell, developed by ELGER AND HESS and described previously.[16] The *operando* cell allows UV-VIS and Raman spectra to be recorded in a defined gas atmosphere while the sensor transducer is heated by its integrated heating meander. Contacts integrated into the cell allow the DC resistance between the electrodes of the transducer to be tapped by a four-point measurement, as well as applying a voltage to the heating meander. The DC resistance is measured by a multimeter (Modell 2000, Keithley); the voltage is applied by a programmable power supply unit (PSP 1803, Voltcraft). To extend the measurement range of the multimeter, a 100 MΩ parallel resistor was used, and the measured resistance of the sensor transducer was calculated from the total resistance using Kirchhoff's circuit laws (see Eq 1).

$$R_{\text{sensor}} = \left(\frac{1}{R_{\text{total}}} - \frac{1}{R_{\text{parallel}}} \right)^{-1} \quad (1)$$

A defined gas atmosphere is created by feeding the following gases (Westfalen AG) into the reaction chamber of the cell and by adjusting their volume flow via mass flow controllers (Bronkhorst): oxygen 5.0 ($\leq$ 0.2 ppm CO_2, $\leq$ 0.2 ppm C_nH_m, $\leq$ 3 ppm H_2O, $\leq$ 10 ppm N_2+ Ar),

nitrogen 5.0 (≤ 3 ppm O_2, ≤ 1 ppm C_nH_m, ≤ 5 ppm H_2O), and 1000 ppm ethanol in nitrogen 5.0. The cell is connected to 1/8-inch stainless steel tubing on the inlet and outlet sides of the cell via Swagelok fittings. A stainless-steel attachment with a quartz glass window (Suprasil; Heraeus) in the center is integrated in the upper Teflon block. For the UV-VIS measurements, a UV-VIS probe can be inserted into the measuring cell through the same stainless-steel attachment. The UV-VIS probe is positioned at a 45° angle to the sample surface. It is used for diffuse reflectance UV-VIS spectroscopy and is connected by a glass fiber to a UV-VIS spectrometer (AvaSpec-ULS2048x14-USB2, Avantes), used in diffuse reflection mode, and a combined D_2 and halogen light source (Avalight-DH-S-DUV-LL, Avantes). Magnesium oxide (Sigma-Aldrich) placed on a sensor transducer in the same position as the sensor was used as the white standard. The sampling time was 60 s, resulting from 500 ms exposure time and averaging 120 spectra.

The sensors installed in the custom-made reaction cell were exposed to a series of gas atmospheres and operation temperatures between 100 and 250 °C. After baking out in synthetic air (80% N_2 + 20% O_2) at 400 °C for 20 min, the sensor was cooled to the desired working temperature for 40 min, followed by a 40 min exposure first to 250 ppm ethanol in the selected carrier gas (synthetic air or nitrogen) and then to the bare carrier gas. While this temperature program was being run in different gas phases, the DC resistance was measured continuously every second and the UV-VIS spectra every 60 s.

3. Results & Discussion

Before deposition of the sensor material on the sensor transducers, the $LaFeO_3$ and $SmFeO_3$ powder samples were characterized by X-ray diffraction (XRD) and Raman spectroscopy. Both XRD and Raman spectra confirm the identity of the used $LaFeO_3$ and $SmFeO_3$ powder materials, showing the expected diffraction peaks (Fig. S1) and lattice phonons (Fig. S2) for $LaFeO_3$ and $SmFeO_3$ when compared to Raman spectra[21] and XRD patterns[22,23] in literature.

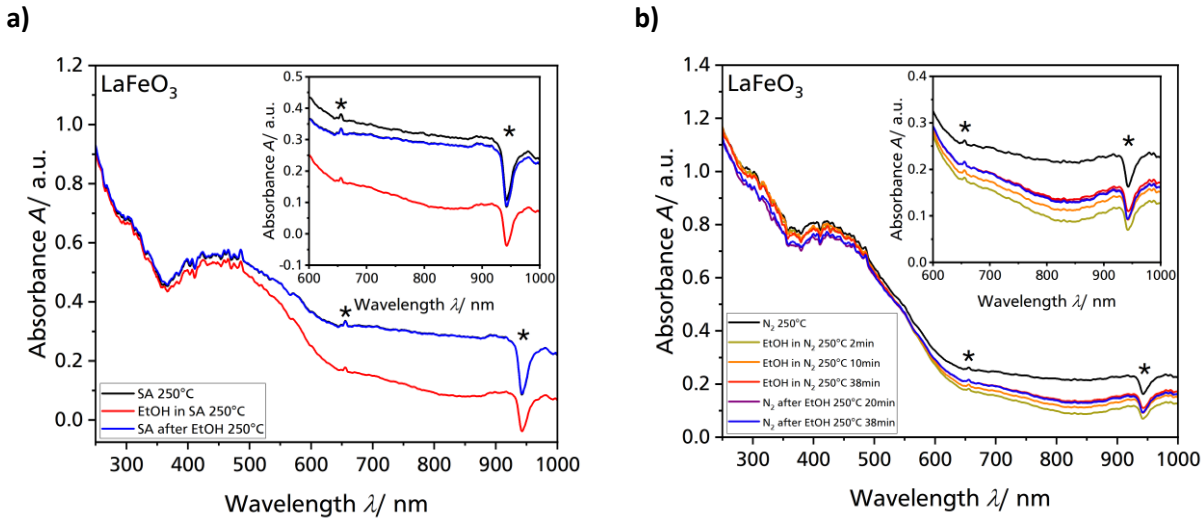

Figure 1. *Operando* UV-VIS spectra of $LaFeO_3$ sensor layer during ethanol sensing at 250 °C using a) synthetic air (80 Vol.-% N_2 + 20 Vol.-% O_2) and b) nitrogen as the carrier gas (total flow rate: 100 ml·min^{-1}). After baking out at 400 °C, the sensor was cooled down to 100 °C (black spectrum). Afterward, 250 ppm of ethanol was added for 40 min (red spectrum), followed by exposure to the respective carrier gas (blue spectrum). In the case of N_2 as the carrier gas, spectra after 2 and 10 min of ethanol exposure, as well as 20 min after ethanol exposure in nitrogen, are also shown. An enlarged view of the region 600-1000 nm is found in the upper right corner of a) and b) for better visualization of the changes in free charge carrier absorption due to changes in the gas atmosphere. The asterisks (∗) mark artifacts of the spectrometer.

Figures 1 and 2 depict UV-VIS spectra recorded at 250 °C for $LaFeO_3$ (Fig. 1) and $SmFeO_3$ (Fig. 2). In synthetic air (Fig. 1a), during ethanol exposure no change is observed for $LaFeO_3$ in the region of the fundamental absorption maximum. For band tailing in the region of the absorption edge, an overall decrease in absorbance is observed, but no shift in the absorption edge, which would hint at a Burstein–Moss shift.[24] This decrease in intensity continues for $LaFeO_3$ from about 500 nm over the entire region below the absorption edge, shown here up to 1000 nm. In this particular region of the spectra, mainly free carrier absorption is expected.[24] This range from 600 nm to 1000 nm is shown enlarged as inset in Figs. 1 and 2, to visualize the small changes in free carrier absorption for $SmFeO_3$ due to changes in the gas atmosphere.

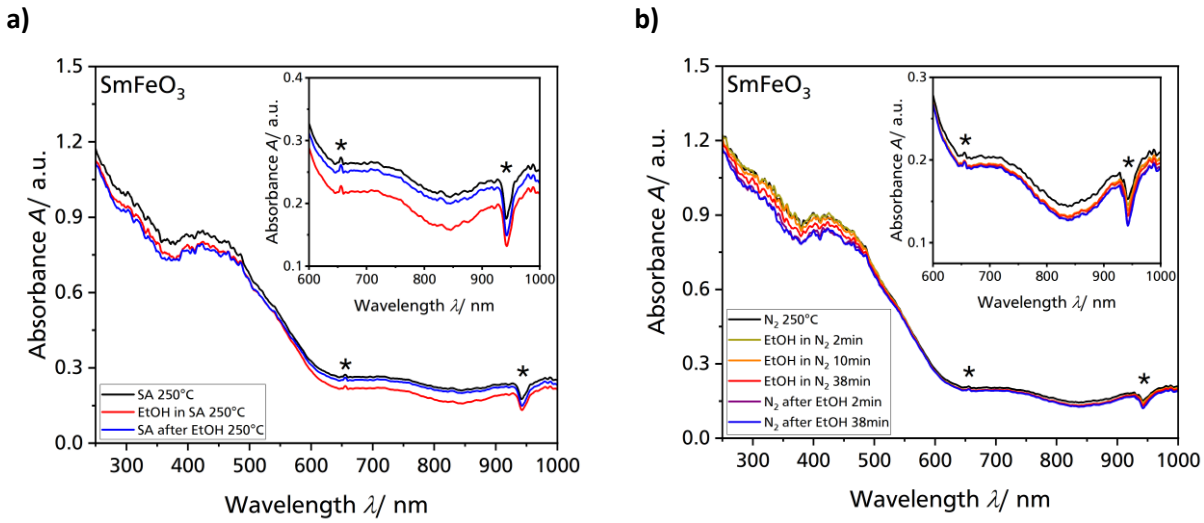

Figure 2. *Operando* UV-VIS spectra of $SmFeO_3$ sensor layer during ethanol sensing at 250 °C using a) synthetic air (80 Vol.-% N_2 + 20 Vol.-% O_2) and b) nitrogen as the carrier gas (total flow rate: 100 ml·min^{-1}). After baking out at 400 °C, the sensor was cooled down to 100 °C (black spectrum). Afterward, 250 ppm of ethanol was added for 40 min (red spectrum), followed by exposure to the respective carrier gas (blue spectrum). In the case of N_2 as the carrier gas, spectra after 2 and 10 min of ethanol exposure, as well as 20 min after ethanol exposure in nitrogen, are also shown. An enlarged view of the region 600-1000 nm is found in the upper right corner of a) and b) for better visualization of the changes in free charge carrier absorption due to changes in the gas atmosphere. The asterisks (∗) mark artifacts of the spectrometer.

A similar behavior like shown before for $LaFeO_3$ is also observed for $SmFeO_3$ (Fig. 2a) when using synthetic air as a carrier gas. No changes are observed for the absorption maximum and the band tailing of the absorption edge up to 600 nm. However, above 600 nm up to 1000 nm, a decrease in free carrier absorption is observed, like for $LaFeO_3$ before, but to a lower extent when compared to $LaFeO_3$. After the end of the ethanol exposure, both $LaFeO_3$ and $SmFeO_3$ show a renewed increase in absorbance in the 600–1000 nm range. At 250 °C, the change in absorbance is completely reversible for $LaFeO_3$ and almost reversible for $SmFeO_3$. At lower temperatures, these changes in absorbance are either irreversible (100-150 °C, see Figs. S3-S6) or only slightly reversible (200 °C, see Figs. S7 and S8). A reversible change in absorbance in the visible and near-

infrared region below the band edge, like observed here for p-type $LaFeO_3$ and $SmFeO_3$, has already been reported under *in situ* as well as *operando* conditions for chemiresistive n-type semiconducting metal oxide gas sensors. For SnO_2, a reversible increase in absorbance was observed during both ethanol[16] and CO[17] gas sensing, representing the exact opposite of the behavior detected here for p-type $LaFeO_3$ and $SmFeO_3$ gas sensors. These reversible changes in absorbance have been attributed to changes in the concentration of free electrons in the conduction band resulting from the formation and ionization of oxygen vacancies.[25] A decrease in absorbance has been observed previously for NiO during optical CO gas sensing, and attributed to a change in the concentration of free electron holes in the valence band.[6,8]

When nitrogen is used as the carrier gas (see Fig. 1b and Fig. 2b), a decrease in absorbance in the 600–1000 nm range is also observed during ethanol exposure, for both $LaFeO_3$ and $SmFeO_3$. However, this decrease in absorbance is irreversible at the same operation temperature as the ethanol exposure before in synthetic air, since at most a very low concentration of oxygen (<3ppm) is present after ethanol exposure to reoxidize the metal oxides when using only nitrogen as a carrier gas. It is noteworthy that the decrease in absorbance during ethanol exposure is not steady for either material. At the beginning, a decrease in absorbance is observed (see dark yellow spectrum), but after a few minutes, there is a renewed increase in absorbance, despite the same reaction conditions (see orange/red spectrum). To illustrate this behavior, Figs. 1b) and 2b) show several spectra during and after ethanol exposure. Furthermore, after ethanol exposure, another weak decrease in absorbance is observed (see purple/blue spectrum), instead of the expected weak increase. Since the observed effects in the range from 600 to 1000 nm are much more pronounced for $LaFeO_3$ than for $SmFeO_3$, we will focus on $LaFeO_3$ in the following, but the corresponding data for $SmFeO_3$ can be found in the Supporting Information (see Figs. S9 and S11).

Figure 3 depicts the temporal evolution of the conductance G as the reciprocal of the DC resistance R and the absorbance A at 800 nm as a measure of the free carrier absorption, enabling a direct comparison of their temporal behavior as a function of gas-phase composition and temperature. For synthetic air as the carrier gas (see Fig. 3a), qualitatively, an identical course is observed for the conductance G and the absorbance A over all phases and temperatures.

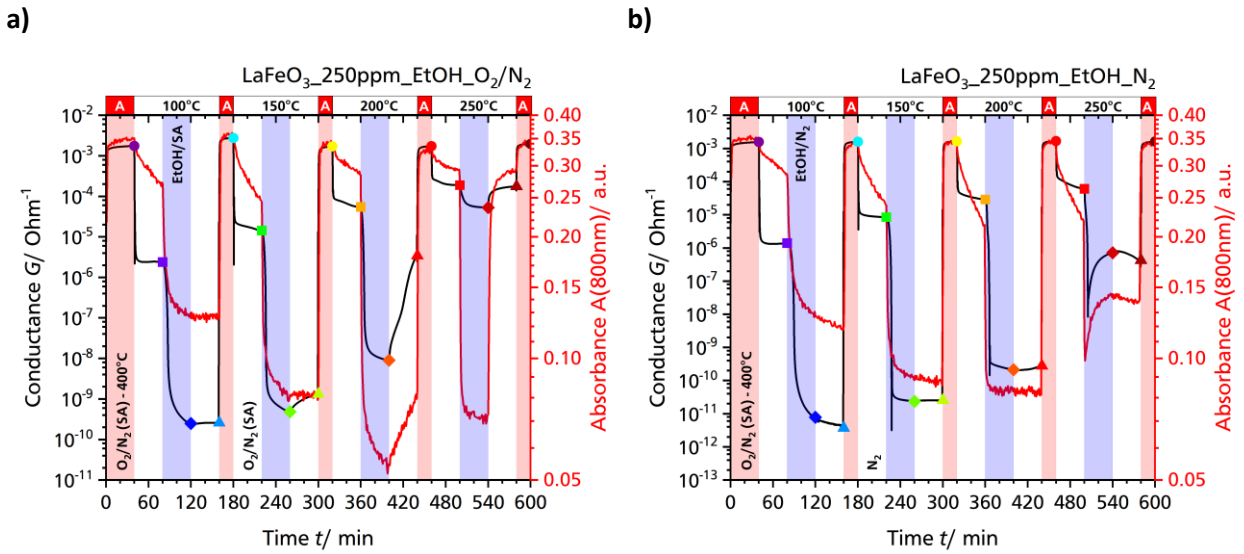

Figure 3. Conductance G and absorbance A (at 800 nm) of the $LaFeO_3$ sensor during O_2/N_2, N_2 and ethanol exposure using a) synthetic air and b) nitrogen as the carrier gas (total flow rate: 100 mL·min^{-1}). Red areas: heating at 400 °C in synthetic air; white areas: sensor at operating temperature in the respective carrier gas; blue areas: exposure to 250 ppm ethanol in the respective carrier gas. The colored symbols mark the final conductivity values for each phase and serve as an orientation for Fig. 4; SA: synthetic air, EtOH: ethanol.

As expected for a p-type semiconductor, both quantities show a decrease during cooling down and ethanol exposure, while regeneration of the sensor material at 200 and 250 °C as well as elevated temperatures (400 °C) leads to an increase.

Similarly, for nitrogen as the carrier gas (see Fig. 3b), there is a qualitative resemblance of the observed conductance and absorbance behavior. Due to the almost complete absence of oxygen in

the gas phase (<3 ppm O_2), the changes are not reversible at 100 °C and 150 °C, and at 200 °C only a weak increase in conductance is observed after the ethanol exposure, but no renewed increase in absorbance at 800 nm. In comparison to the oxygen-rich conditions this clearly shows that at these lower temperatures (100-200 °C) oxygen is necessary for both a reversible electrical as well as optical sensor response, which was not clear from the measurements in oxygen-rich conditions alone. During exposure to ethanol and the carrier gas at 250 °C, the conductance and absorbance at 600–1000 nm show a behavior that differs significantly from that between 100 °C and 200 °C. At the beginning of the ethanol exposure at 250 °C, the conductance shows a decrease as expected for a p-type semiconductor, but then, surprisingly, an increase is detected. Such a behavior was not observed for $LaFeO_3$ at 250 °C under oxygen-rich conditions. After the ethanol exposure in nitrogen, no renewed increase is observed, but rather a decrease in conductance, which is characteristic of an n-type semiconductor. This indicates that under such strongly reducing conditions in the almost complete absence of oxygen at 250°C, a p-n transition occurs for $LaFeO_3$. Such a transition was observed experimentally for α-Fe_2O_3[26] and predicted theoretically for $LaFeO_3$[27] and other perovskites at low oxygen partial pressures.[28] The majority charge carriers under these conditions are no longer electron holes, which are neutralized by the consumption of oxygen species and the release of electrons,[15] but electrons themselves. Consequently, the electrical conductivity and the free carrier absorption are significantly influenced. The absorption of free charge carriers is given by Eq. 2.[29]

$$\alpha_{\mathrm{FCA}} = \frac{Nq^2\lambda^2}{4\pi^2\varepsilon_0 m_c c^3 n\tau} = \left(\frac{e^3\lambda^2}{4\pi^2 c^3 n\varepsilon_0}\right)\left(\frac{N_{e'}}{m_{\dot{e}}^2\mu_{e'}} + \frac{N_{h^{\cdot}}}{m_{\dot{h}}^2\mu_{h^{\cdot}}}\right) \quad (2)$$

Here, α_{FCA} is the absorption coefficient of free carrier absorption, N_{i} the concentration of free charge carriers, λ the wavelength of the irradiating light, ε_0 the vacuum permittivity, m_{c} the effective mass of the majority charge carrier, n the refractive index, τ the mean free time, and μ_{i} the mobility of the free charge carrier. Since usually either electrons or electron holes have a concentration several orders of magnitude higher than the other species, the contribution of one of the charge carriers dominates. If the simple Drude model[24] is used to describe the electrical conductivity σ, a qualitative agreement of the conductance and absorbance changes is expected, since both quantities are proportional to each other (Eq. 3), fully consistent with the experimental observations. Both quantities are dependent on the concentration of the majority charge carrier N, which changes due to the reaction of ethanol with the sensor surface, since oxygen species are consumed at the surface.[11,30]

$$\frac{1}{R} = G \sim \sigma = \frac{N \cdot e^2 \cdot \tau}{m_c} \sim A \sim \alpha_{\mathrm{FCA}} = \frac{Nq^2\lambda^2}{4\pi^2\varepsilon_0 m_c c^3 n\tau} \quad (3)$$

Although there is good qualitative agreement between the free carrier absorption and the conductance curves, upon closer inspection, distinct differences become apparent. In fact, when comparing the course of both quantities in Fig. 3, it is noticeable that the absolute values of the conductance and absorbance do not show a uniform trend from temperature to temperature. To investigate this aspect more closely, Fig. 4 shows the absorbance against the median of the conductance G over one minute in a double logarithmic plot.

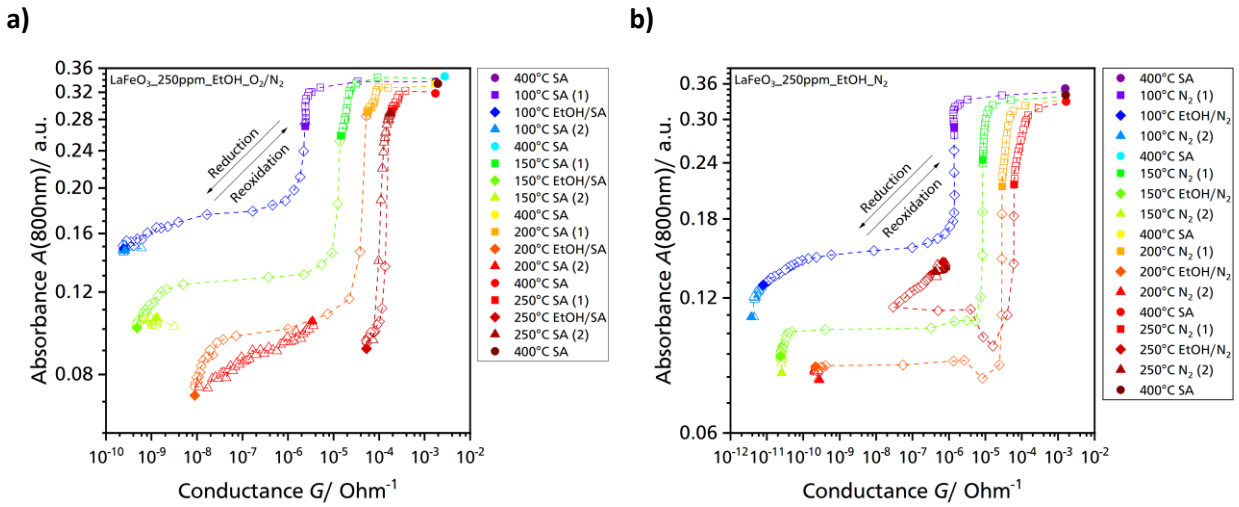

Figure 4. Double logarithmic plot of the absorbance *A* at 800 nm as a function of the conductance *G* for the $LaFeO_3$ sensor using a) synthetic air (SA) and b) N_2 as the carrier gas (total flow rate: 100 mL·min^{-1}) during (i) heating out in synthetic air at 400 °C (circles), (ii) cooling down to operation temperature (squares), (iii) exposure to 250 ppm ethanol (EtOH) (diamonds) and (iv) reoxidation after ethanol exposure (triangles). The median value for a time interval of 1 min was plotted for the conductance in each case. The last data point of each phase is marked by a filled-in symbol; the different temperatures are indicated by the different colors of the symbols. For clarity, the number of data points has been reduced (for all data points, see Fig. S10).

According to Eq. 3, pairs of values would be expected to fall on a straight line. Figure 4 clearly shows that this is not the case, neither for synthetic air nor for nitrogen as the carrier gas. The data points at the end of the bakeout (circles) and the ethanol exposure (diamonds) phase would serve as endpoints of such a line but are rather connected by a sigmoidal curve (see Fig. 4). At the beginning of the cooling phase (squares), first the conductance shows a rapid decrease with otherwise almost constant absorbance before the change in absorbance occurs with a time lag. At the beginning of the ethanol exposure (diamond), on the other hand, the absorbance first shows a sudden decrease before the conductance undergoes a significant change. This difference in the

response time indicates that, in addition to the change in N, another process needs to be considered that affects conductance and absorbance to different degrees. Moreover, this process appears to be temperature dependent since the endpoints of ethanol exposure do not lie on the theoretically expected line. From 100 °C to 200 °C, the absorbance decreases in relative terms compared to the increasing conductivity. Only for a temperature increase from 200 °C to 250 °C do the absorbance and the conductance increase again, both for synthetic air and for nitrogen as the carrier gas. This additional effect, which significantly influences the conductivity of the sensor material but plays only a minor role for the free carrier absorption, originates from the formation of a hole accumulation layer towards the surface, resulting in back-to-back Schottky barriers between the grains of the sintered sensor material.[30] The height of these potential barriers eV_s significantly determines the conductivity and undergoes changes due to the consumption of surface oxygen species and the formation of adsorbate species (e.g., formate).[4,15] As a consequence, the conductivity of surface-near layers dominates the conductivity of the entire grain. A quantitative description of the total conductivity of a p-type semiconductor has been developed by BARSAN *et al.*[30] and is shown in Eq. 4:

$$R = R_B \cdot \left(\frac{L_D}{D_C} \cdot exp\left(-\frac{qV_s}{2kT}\right) + \frac{1}{1 + \frac{L_D}{D_G} \cdot exp\left(\frac{qV_s}{2kT}\right)} \right) \tag{4}$$

Here R_B is the electrical bulk resistance, L_D the Debye length, D_C the effective contact area between grains, D_G the effective grain size, q the charge of the majority charge carrier, V_s the surface potential, k the Boltzmann constant and T the temperature. Equation 4 clearly shows that, in addition to the electrical bulk resistance, to which Drude's model can be applied, the height of

Schottky barriers eV_S determines the absolute value of the DC resistance via the exponential Boltzmann terms, thus underlining the important influence of surface effects on the total conductivity. The free carrier absorption, on the other hand, is mainly influenced by N, and thus correlates more with the bulk resistance, which is only one contribution to the total sensor resistance.

4. Conclusions

Using time-resolved *operando* UV-VIS spectroscopy we were able to simultaneously investigate the electrical and optical properties of $LaFeO_3$ and $SmFeO_3$ gas sensors. The qualitative match of the conductance and absorbance behavior of $LaFeO_3$ and $SmFeO_3$ at 600–1000 nm can be attributed to changes in the free carrier concentration, which are involved in the sensor mechanism of chemiresistive and gasochromic gas sensors, as demonstrated here for $LaFeO_3$ and $SmFeO_3$. The involvement of free charge carriers in both sensing mechanisms was further supported by the observed p-n transition. Quantitative differences in the temporal development of conductance and absorbance reveal mechanistic differences between chemiresistive and gasochromic gas sensors. In addition to changes in free carrier absorption, the electrical conductance is strongly influenced by the formation of potential barriers and hole accumulation layers. For the free carrier absorption and the mechanism of gasochromic gas sensors, on the other hand, these potential barriers play only a minor role even though the same surface reactions are taking place in contact with the gas phase.

Our results demonstrate the potential of time-resolved *operando* UV-VIS spectroscopy to discriminate between surface effects and bulk effects in chemiresistive and gasochromic sensors,

thereby enhancing the understanding of both fields of research. Comparing the electrical sensor response (changes in DC resistance) and the optical sensor response (changes in free carrier absorption) gives an indication of whether the sensor mechanism is dominantly based on changes in subsurface areas of the sensor material and the majority charge carrier concentration, as described for a reduction–reoxidation mechanism,[4,16,17] or on changes in adsorbed oxygen species and surface adsorbates, as described for an ionosorption mechanism.[2–4]

Our results can also be the basis for the development of novel gas sensors with enhanced target gas selectivity, based on a fundamental mechanistic understanding. Combining electrical and optical sensor response of one sensor material can lead to an enhanced degree of information, because target gases other than ethanol (e.g., CO, H_2) may lead to varying ratios of the electrical and optical sensor responses resulting from their specific surface adsorbates and reduction potential, thus influencing the electrical and optical sensor responses to different degrees.[31]

ASSOCIATED CONTENT

The following files are available free of charge.

Supporting Information: Additional figures for *ex situ* characterization (Raman, XPS) and time-resolved *operando* UV-VIS spectroscopy of $LaFeO_3$ and $SmFeO_3$ (PDF).

AUTHOR INFORMATION

Corresponding Author

*e-mail: christian.hess@tu-darmstadt.de

Author Contributions

The manuscript was written through contributions of all authors. All authors have given approval to the final version of the manuscript.

Notes

The authors declare no competing financial interests.

ACKNOWLEDGMENTS

The authors thank Kathrin Hofmann for XRD measurements. We also thank Benjamin Junker (Institute of Physical and Theoretical Chemistry (IPTC), University of Tuebingen) for providing the $LaFeO_3$ and $SmFeO_3$ powder samples, and Joanna Müller for preliminary joint work on perovskite gas sensors using steady-state *operando* Raman/UV-VIS spectroscopy. This research was funded by the Deutsche Forschungsgemeinschaft (DFG, HE 4515/6-3).

REFERENCES

(1) Gomes, J. B. A.; Rodrigues, J. J. P. C.; Rabêlo, R. A. L.; Kumar, N.; Kozlov, S. IoT-Enabled Gas Sensors: Technologies, Applications, and Opportunities. *J. Sens. Actuator Netw.* **2019**, *8*, 57.

(2) Neri, G. First Fifty Years of Chemoresistive Gas Sensors. *Chemosensors* **2015**, *3*, 1–20.

(3) Tiemann, M. Porous metal oxides as gas sensors. *Chem. Eur. J.* **2007**, *13*, 8376–8388.

(4) Staerz, A.; Weimar, U.; Barsan, N. Current state of knowledge on the metal oxide based gas sensing mechanism. *Sens. Actuators B: Chem.* **2022**, *358*, 131531–131548.

(5) Kalanur, S. S.; Lee, Y.-A.; Seo, H. Eye-readable gasochromic and optical hydrogen gas sensor based on CuS–Pd. *RSC Adv.* **2015**, *5*, 9028–9034.

(6) Zbroniec, L.; Martucci, A.; Sasaki, T.; Koshizaki, N. Optical CO gas sensing using nanostructured NiO and NiO/SiO_2 nanocomposites fabricated by PLD and sol–gel methods. *Appl. Phys. A* **2004**, *79*, 1303–1305.

(7) Staerz, A.; Somacescu, S.; Epifani, M.; Kida, T.; Weimar, U.; Barsan, N. WO_3-Based Gas Sensors: Identifying Inherent Qualities and Understanding the Sensing Mechanism. *ACS Sens.* **2020**, *5*, 1624–1633.

(8) Çoban, Ö.; Tekmen, S.; Gür, E.; Tüzemen, S. High optical response NiO, Pd/NiO and Pd/WO_3 hydrogen sensors. *Int. J. Hydrogen Energy* **2022**, *47*, 25454–25464.

(9) Grätzel, M. The light and shade of perovskite solar cells. *Nat. Mater.* **2014**, *13*, 838–842.

(10) Taylor, F. H.; Buckeridge, J.; Catlow, C. R. A. Defects and Oxide Ion Migration in the Solid Oxide Fuel Cell Cathode Material $LaFeO_3$. *Chem. Mater.* **2016**, *28*, 8210–8220.

(11) Alharbi, A.; Junker, B.; Alduraibi, M.; Algarni, A.; Weimar, U.; Bârsan, N. The Role of Different Lanthanoid and Transition Metals in Perovskite Gas Sensors. *Sensors* **2021**, *21*, 8462–8472.

(12) Alharbi, A. A.; Sackmann, A.; Weimar, U.; Bârsan, N. A highly selective sensor to acetylene and ethylene based on $LaFeO_3$. *Sens. Actuators B: Chem.* **2020**, *303*, 127204–127212.

(13) Li, F.; Lv, Q.; Gao, L.; Zhong, X.; Zhou, J.; Gao, X. Ultra-sensitive Ag-$LaFeO_3$ for selective detection of ethanol. *J. Mater. Sci.* **2021**, *56*, 15061–15068.

(14) Sukee, A.; Alharbi, A. A.; Staerz, A.; Wisitsoraat, A.; Liewhiran, C.; Weimar, U.; Barsan, N. Effect of AgO loading on flame-made $LaFeO_3$ p-type semiconductor nanoparticles to acetylene sensing. *Sens. Actuators B: Chem.* **2020**, *312*, 127990–128000.

(15) Kim, H.-J.; Lee, J.-H. Highly sensitive and selective gas sensors using p-type oxide semiconductors: Overview. *Sens. Actuators B: Chem.* **2014**, *192*, 607–627.

(16) Elger, A.-K.; Hess, C. Elucidating the Mechanism of Working SnO_2 Gas Sensors Using Combined Operando UV/Vis, Raman, and IR Spectroscopy. *Angew. Chem. Int. Ed.* **2019**, *58*, 15057–15061.

(17) Degler, D.; Barz, N.; Dettinger, U.; Peisert, H.; Chassé, T.; Weimar, U.; Barsan, N. Extending the toolbox for gas sensor research: Operando UV/vis diffuse reflectance spectroscopy on SnO_2-based gas sensors. *Sens. Actuators B: Chem.* **2016**, *224*, 256–259.

(18) Schilling, C.; Hess, C. CO Oxidation on Ceria Supported Gold Catalysts Studied by Combined Operando Raman/UV–Vis and IR Spectroscopy. *Top. Catal.* **2017**, *60*, 131–140.

(19) Ziemba, M.; Hess, C. Influence of gold on the reactivity behaviour of ceria nanorods in CO oxidation: combining operando spectroscopies and DFT calculations. *Catal. Sci. Technol.* **2020**, *10*, 3720–3730.

(20) Ziemba, M.; Schumacher, L.; Hess, C. Reduction Behavior of Cubic In_2O_3 Nanoparticles by Combined Multiple In Situ Spectroscopy and DFT. *J. Phys. Chem. Lett.* **2021**, *12*, 3749–3754.

(21) Weber, M. C.; Guennou, M.; Zhao, H. J.; Íñiguez, J.; Vilarinho, R.; Almeida, A.; Moreira, J. A.; Kreisel, J. Raman spectroscopy of rare-earth orthoferrites $RFeO_3$ (R =La, Sm, Eu, Gd, Tb, Dy). *Phys. Rev. B* **2016**, *94*, 214103-214110.

(22) Jain, P.; Srivastava, S.; Baroliya, I.; Gupta, N. Structure and particle size analysis of $LaFeO_3$ nanoparticles. *AIP Conf. Proc.* **2016**, *1728*, 20659–20662.

(23) Gaiardo, A.; Zonta, G.; Gherardi, S.; Malagù, C.; Fabbri, B.; Valt, M.; Vanzetti, L.; Landini, N.; Casotti, D.; Cruciani, G.*; et al.* Nanostructured $SmFeO_3$ Gas Sensors: Investigation of the Gas Sensing Performance Reproducibility for Colorectal Cancer Screening. *Sensors* **2020**, *20*, 5910–5923.

(24) Dresselhaus, M.; Dresselhaus, G.; Cronin, S.; Gomes Souza Filho, A. *Solid State Properties: From Bulk to Nano*; Springer: Berlin, Heidelberg, 2018; pp 131-133, 374-375, 457.

(25) Amalric Popescu, D.; Herrmann, J.-M.; Ensuque, A.; Bozon-Verduraz, F. Nanosized tin dioxide: Spectroscopic (UV–VIS, NIR, EPR) and electrical conductivity studies. *Phys. Chem. Chem. Phys.* **2001**, *3*, 2522–2530.

(26) Gurlo, A.; Bârsan, N.; Oprea, A.; Sahm, M.; Sahm, T.; Weimar, U. An n- to p-type conductivity transition induced by oxygen adsorption on α-Fe_2O_3. *Appl. Phys. Lett.* **2004**, *85*, 2280–2282.

(27) Mutter, D.; Schierholz, R.; Urban, D. F.; Heuer, S. A.; Ohlerth, T.; Kungl, H.; Elsässer, C.; Eichel, R.-A. Defects and Phase Formation in Non-Stoichiometric $LaFeO_3$: a Combined Theoretical and Experimental Study. *Chem. Mater.* **2021**, *33*, 9473–9485.

(28) Singh, K.; Nowotny, J.; Thangadurai, V. Amphoteric oxide semiconductors for energy conversion devices: a tutorial review. *Chem. Soc. Rev.* **2013**, *42*, 1961–1972.

(29) Trevor S. Moss. *Optical properties of Semi-Conductors*, Repr. and rev. Ed.; Semi-Conductor Monographs; Butherworths: London, 1961; pp 29-30.

(30) Barsan, N.; Simion, C.; Heine, T.; Pokhrel, S.; Weimar, U. Modeling of sensing and transduction for p-type semiconducting metal oxide based gas sensors. *J. Electroceram.* **2010**, *25*, 11–19.

(31) Girma, H. G.; Lee, H. M.; Kim, Y.; Ryu, G.-S.; Jeon, S.; Kim, J. Y.; Jung, S.-H.; Kim, S. H.; Noh, Y.-Y.; Lim, B. Highly sensitive and wrappable room temperature wireless gasochromic and chemiresistive dual-response H_2 sensors using spray coating. *Nano Energy* **2023**, *113*, 108551.

TOC Graphic

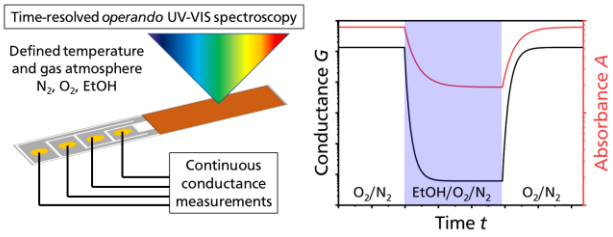
Time-resolved *operando* UV-VIS spectroscopy
Defined temperature and gas atmosphere
N_2, O_2, EtOH
Continuous conductance measurements
Conductance *G*
Absorbance *A*
O_2/N_2
EtOH/O_2/N_2
O_2/N_2
Time *t*